Supporting information

Exploring the preparation-dependence of crystalline 2D-extended ultrathin C8-BTBT-C8 films

*Tim Hawly [a], ‡ Manuel Johnsonb[a], ‡ Andreas Späth [a], Hannah Nickles Jäkel [a], Mingjian Wu [b], Erdmann Spiecker [b], Benjamin Watts [c], Alexei Nefedov [d]† and Rainer H. Fink [a]**

[a] Friedrich-Alexander-Universität Erlangen-Nürnberg, Department Chemie und Pharmazie, Egerlandstraße 3, 91058 Erlangen, Germany

[b] Friedrich-Alexander-Universität Erlangen-Nürnberg, Institute of Micro- and Nanostructure Research, Cauerstraße 3, 91058 Erlangen, Germany

[c] Paul Scherrer Institute, Villigen 5232, Switzerland

[d] Institute of Functional Interfaces (IFG), Karlsruhe Institute of Technology (KIT), 76344 Eggenstein-Leopoldshafen, Germany.

*Corresponding author:

Rainer H. Fink, Friedrich-Alexander-Universität Erlangen-Nürnberg, Physical Chemistry II, Egerlandstraße 3, 91058 Erlangen, Germany, E-mail: rainer.fink@fau.de

S1 – Charge-transport parameters of fabricated C8-BTBT-C8 OFETs S3
S1-1 – Thermal evaporation S3
S1-2 – Dropcasting S4
S1-3 – Liquid-liquid processing S5
S2 – Influence of varying substrate inclination angles on the thin-film morphology S6
S3 – Scanning transmission x-ray microscopy S7
S3-1 – Generation of molecular orientation contrast in STXM S7
S3-2 – In-plane azimuthal dependence in liquid-liquid processed C8-BTBT-C8 thin films S9
S4 – Solvent dependence for liquid-liquid processed C8-BTBT-C8 thin films S10
S5 – AFM images of aged toluene and heptane-based C8-BTBT-C8 thin films S11
S6 – NEXAFS fitting procedure and tilt angle derivation for fabricated thin films S12
S6-1 – General procedure S12
S6-2 – Thermal evaporation S13
S6-3 – Dropcasting S14
S6-4 – Liquid-liquid processing S15

S1 – Charge-transport parameters of fabricated C8-BTBT-C8 OFETs

S1-1 – Thermal evaporation

Transfer and output plots of fabricated top-contact bottom-gate OFETs show reproducible charge-transport capability. It is noted that charge-carrier mobility, on/off ratio, and threshold voltage improve upon rising substrate temperatures (T = 333 K) during C8-BTBT-C8 deposition.

This is due to the decisively lower nucleation density accounting for a lower amount of grain boundaries acting as charge traps within the semiconducting layer. Hence, charge transfer, as well as the switching process, takes place within a better defined C8-BTBT-C8 semiconducting junction. Still, extracted charge-transport parameters are considerably worse as compared to drop-casted or liquid-liquid processed specimen.

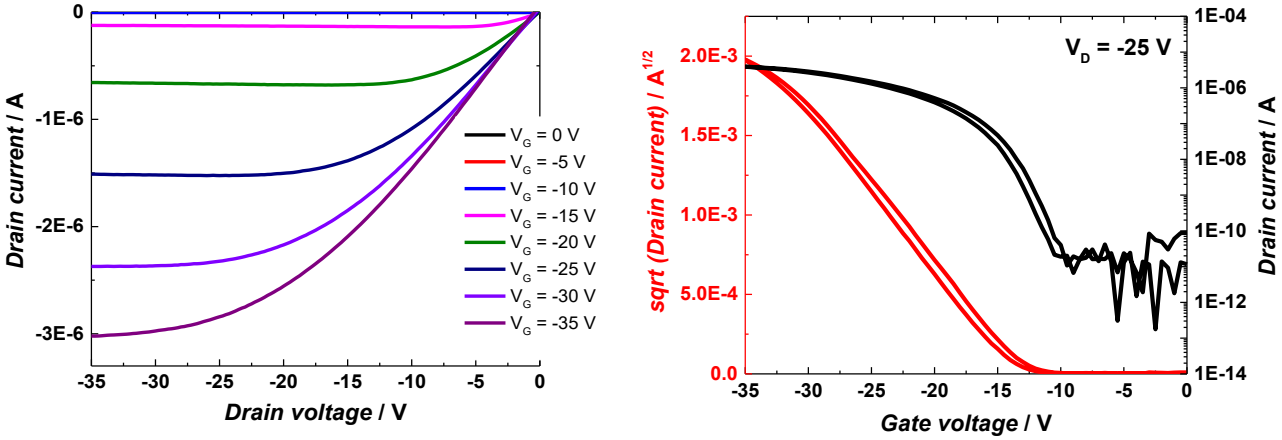

Figure S1. Output (left) and transfer characteristics (right) of OFETs based on a thermally evaporated C8-BTBT-C8 layer.

S1-2 – Dropcasting

We observe drastically improved charge-transport behavior. Hole mobilities as high as 3.59 $cm^2V^{-1}s^{-1}$ and on/off ratios in the high 10^6 regime are observed, which excels reference values from samples fabricated via thermal evaporation (SI1-1) by a factor of 2 and by more than one order in magnitude, respectively. Generally, decent on/off-ratios require a high carrier mobility to yield high on-currents accompanied by a low intrinsic conductivity of the semiconductor to assure low off-currents.

Both criteria are observed for drop-casted structures as elevated charge-carrier mobilities and, especially, low off-currents are obtained (I_{Off} = 2.1 x 10^{-5} µA; thermal evaporation: I_{Off} = 3.3 x 10^{-4} µA). On-currents one order in magnitude larger than for vacuum-processed reference samples are observed, which is indicative of a lower number of grain boundaries within the active semiconducting layer, *i.e.*, a larger number of charge carriers reaches the drain electrode.

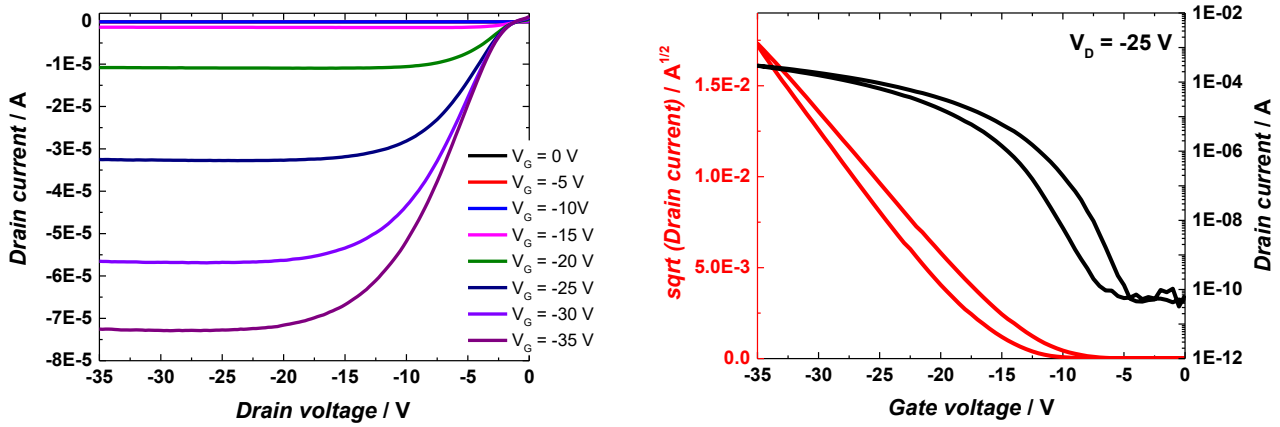

Figure S2. Output (left) and transfer characteristics (right) of a transistor based on a drop-casted C8-BTBT-C8 semiconducting layer.

S1-3 – Liquid-liquid processing

Fabricated top-contact bottom-gate OFETs exhibit excellent charge-transport and switching behavior. Due to the improved, crystalline microstructure of the semiconducting layer, the number of intrinsic grain boundaries, *i.e.,* potential charge traps, is reduced accounting for more efficient hole transport. With respect to entirely vacuum-processed reference samples (SI1-1), we observe maximum hole mobilities increasing by factors of 2.

In addition, maximum on/off ratios increase by one order in magnitude for both compounds, which can be assigned in large part to improving on-currents. In analogy to drop-casted C8-BTBT-C8 films, this can be explained by the well-defined microstructure of the organic layer as a larger number of charge carriers can pass the semiconducting junction between source and drain electrode without hindrance.

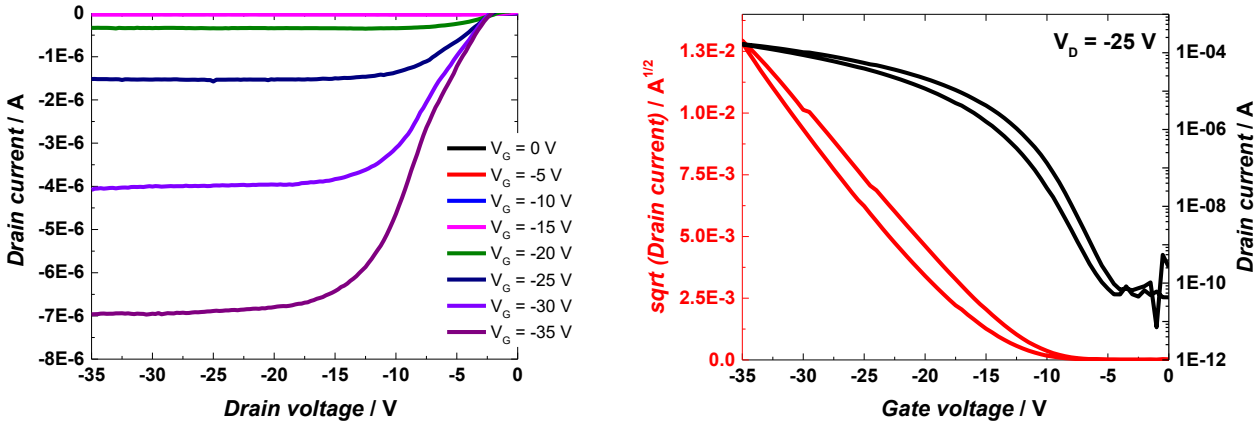

Figure S3. Output (left) and transfer characteristics (right) of a transistor based on a liquid-liquid processed C8-BTBT-C8 semiconducting layer.

S2 – Influence of varying substrate inclination angles on the thin-film morphology

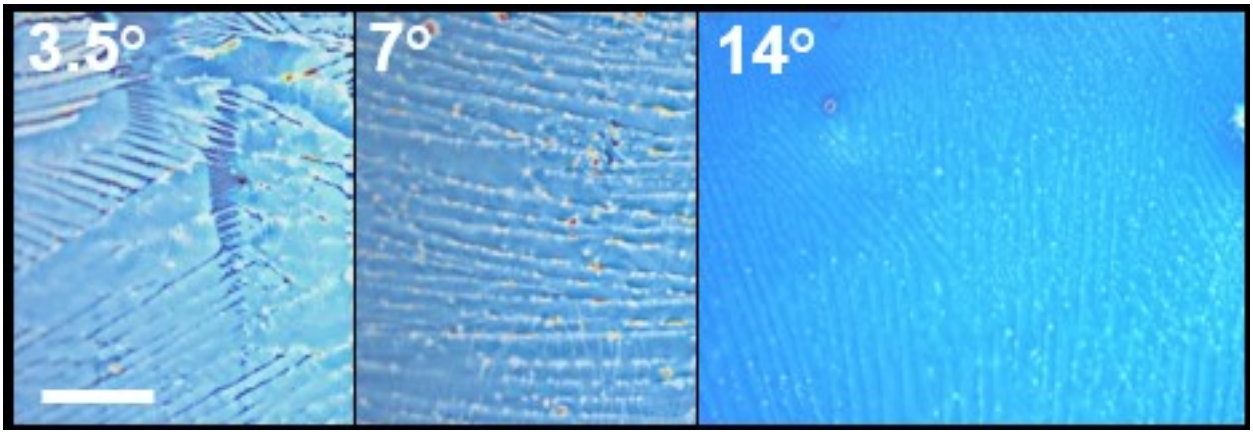

Figure S4. Drop-casted C8-BTBT-C8 thin films from chloroform solution at different substrate inclination angles. Concentration (0.3 mg/ml) and droplet volume (15 µl) were kept constant during the series. The scalebar corresponds to 200 µm for all micrographs.

S3 – Scanning transmission x-ray microscopy

S3-1 – Generation of molecular orientation contrast in STXM

STXM micrographs were recorded at distinct resonant energies corresponding to C1s→π* electronic transitions. Additionally, one micrograph was recorded at photon energy of 320 eV to account for intensity variation due to varying thickness within the film in the data evaluation process. Amongst other parameters such as chemical composition and sample temperature, the transmitted photon flux, I_{trans}, also depends on the thickness of the specimen and the local azimuthal orientation of the final state molecular orbital, *i.e.*, the π* orbital.

$$I_{trans}(x,y,T,h\nu) = I_0(h\nu) * e(-\rho\mu(h\nu,Z)d)$$

To gain microscopic access to the azimuthal orientation of the final state molecular orbital, *i.e.*, molecular orientation contrast, the intensity ratio of a resonant energy image (I) and a micrograph measured at 320 eV (I_0) is considered. By this procedure, contrast contributions due to a varying thickness within the examined section are eliminated and all contrast is due to the molecular orientation.

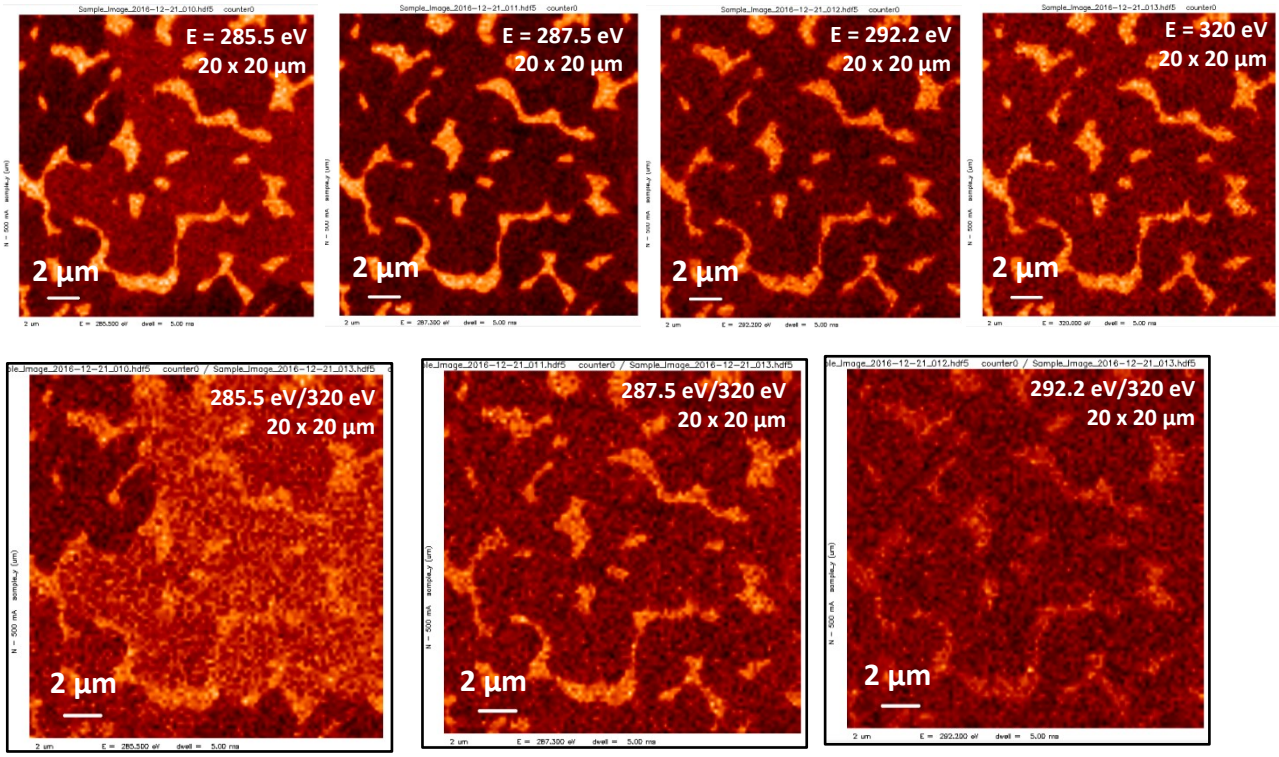

Figure S5. 20 x 20 µm STXM images of thermally evaporated (T = 333 K) C8-BTBT-C8 thin films recorded at varying photon energies, bottom: respective, thickness-corrected images. Note the superior sensitivity regarding molecular orientation contrast in images taken at incident photon energy of 285.5 eV.

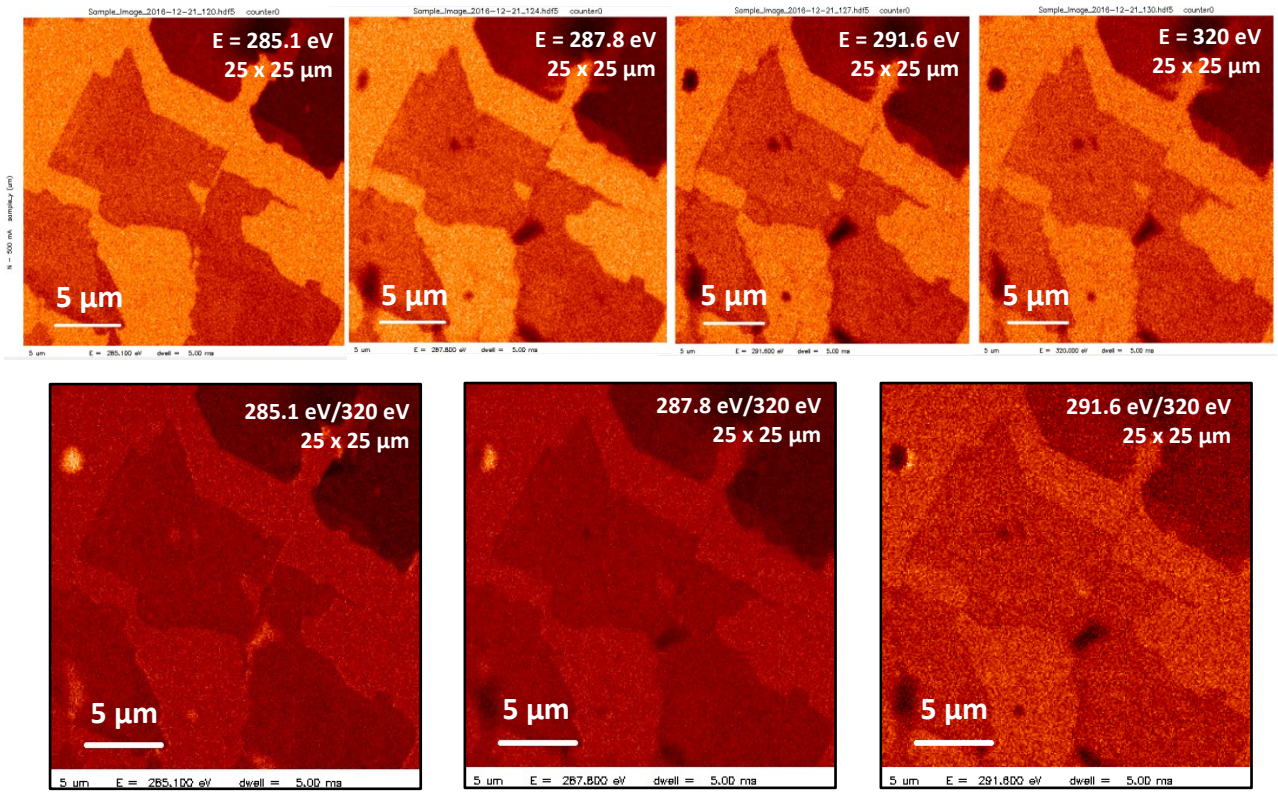

Figure S6. 25 x 25 µm STXM images of drop-casted C8-BTBT-C8 thin films recorded at varying photon energies, bottom: respective, thickness-corrected images. Note the superior sensitivity regarding molecular orientation contrast in images taken at incident photon energy of 285.1 eV.

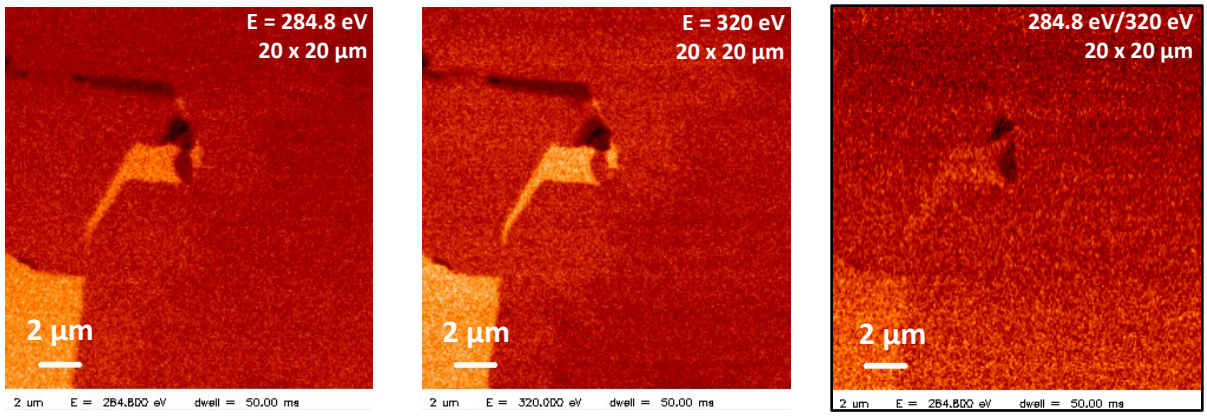

Figure S7. 20 x 20 µm STXM images of liquid-liquid processed C8-BTBT-C8 thin films recorded at varying photon energies (left, middle), and the respective, thickness-corrected image (right). Note the lack of orientation-dependent contrast in the thickness-corrected image, which is indicative of a consistent molecular orientation.

S3-2 – In-plane azimuthal dependence in liquid-liquid processed C8-BTBT-C8 thin films

Liquid-liquid processed thin-film flakes were mapped using STXM and checked regarding their spectral behavior upon azimuthal rotation at normal incidence ($\theta = 90°$). NEXAFS spectra were obtained along the annotated blue line in 15°-steps. We observe clear dichroic effects in the early π* resonance at ≈ 285 eV upon azimuthal rotation confirming the azimuthal anisotropy and high degree of crystallinity within the measured C8-BTBT-C8 film.

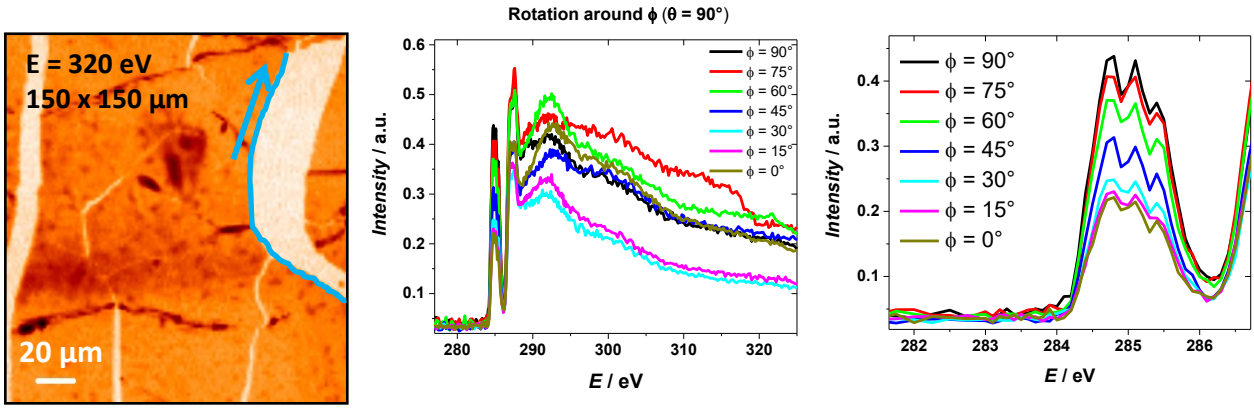

Figure S8. 150 x 150 µm STXM image of a liquid-liquid processed representative C8-BTBT-C8 thin film (left). The corresponding, locally obtained series of NEXAFS spectra (middle) was recorded along the indicated blue line, *i.e.*, they refer to the same flake. The dichroic behavior of the orientation-sensitive π*-resonance at 285 eV upon azimuthal rotation is shown in greater detail on the right.

S4 – Solvent dependence for liquid-liquid processed C8-BTBT-C8 thin films

For samples based on chloroform or chloroform-toluene mixtures, we observe a floating lens on top of the water for solution volumes smaller than 200 µL. For larger amounts the solution droplet sinks towards the bottom of the beaker. Figure 9 displays the solvent dependency for a commonly used 0.3 mg/mL C8-BTBT-C8 original solution. With chloroform being a rapidly evaporating solvent, the molecules are only given an insufficient amount of time for extended self-assembly (a). While a relatively thin, 2D-confined organic layer is forming on the water surface, the structures are only macroscopically closed with single flakes merely excelling diameters of 20 µm. Upon addition of toluene to the original solution the growth behavior changes drastically, and microscopically closed film structures in the range of mm² are observed (b). Solely toluene-based films show similar growth behavior with an increasing tendency towards unfavorable out-of-plane growth (c). Thin films based on an *n*-heptane original solution (d) appeared to distinctly grow as 1D needles in-plane with out-of-plane growth being favored over extended 2D growth, which highlights the importance of solvents capable of interacting with the pi-heavy core units of the semiconductor.

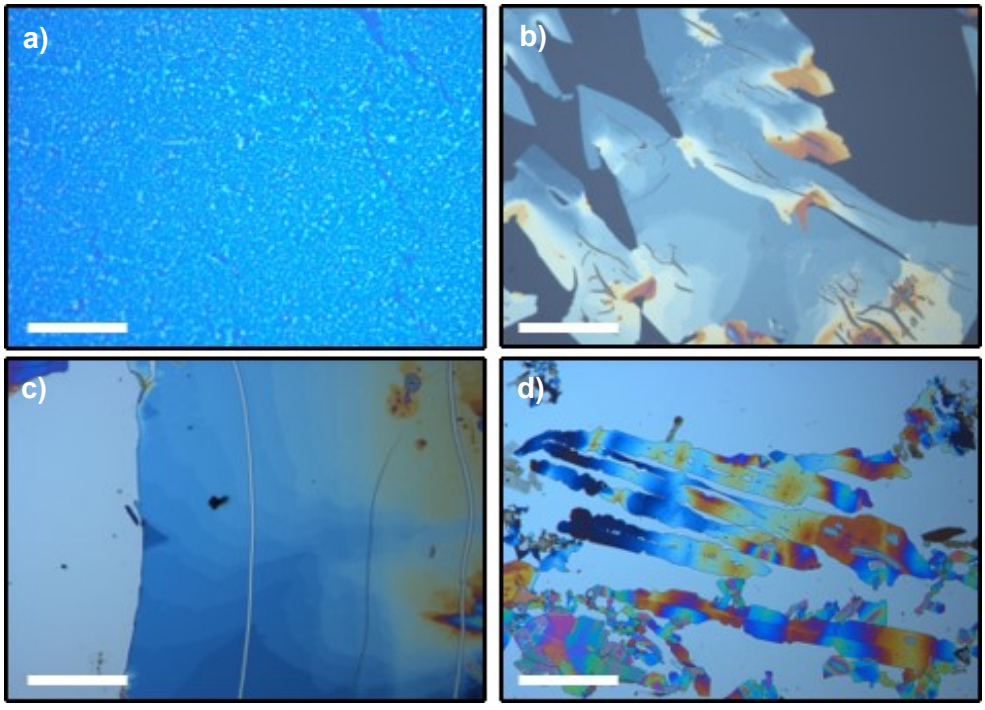

Figure S9. OM images of C8-BTBT-C8 thin films fabricated at the liquid-liquid interface using varying solvents. a) chloroform, b) chloroform-toluene (3:1), c) toluene, d) n-heptane. In all images the scalebar corresponds to 200 µm.

S5 – AFM images of aged toluene and heptane-based C8-BTBT-C8 thin films

AFM micrographs of representative C8-BTBT-C8 thin-film sections were measured both directly and 96 h after deposition via non-contact atomic force microscopy. For toluene-based specimen (a, b), we observe aging effects with developing vacancies within the range of the C8-BTBT-C8 long axis (≈ 3 nm). Heptane-based specimens (c, d) lack such features.

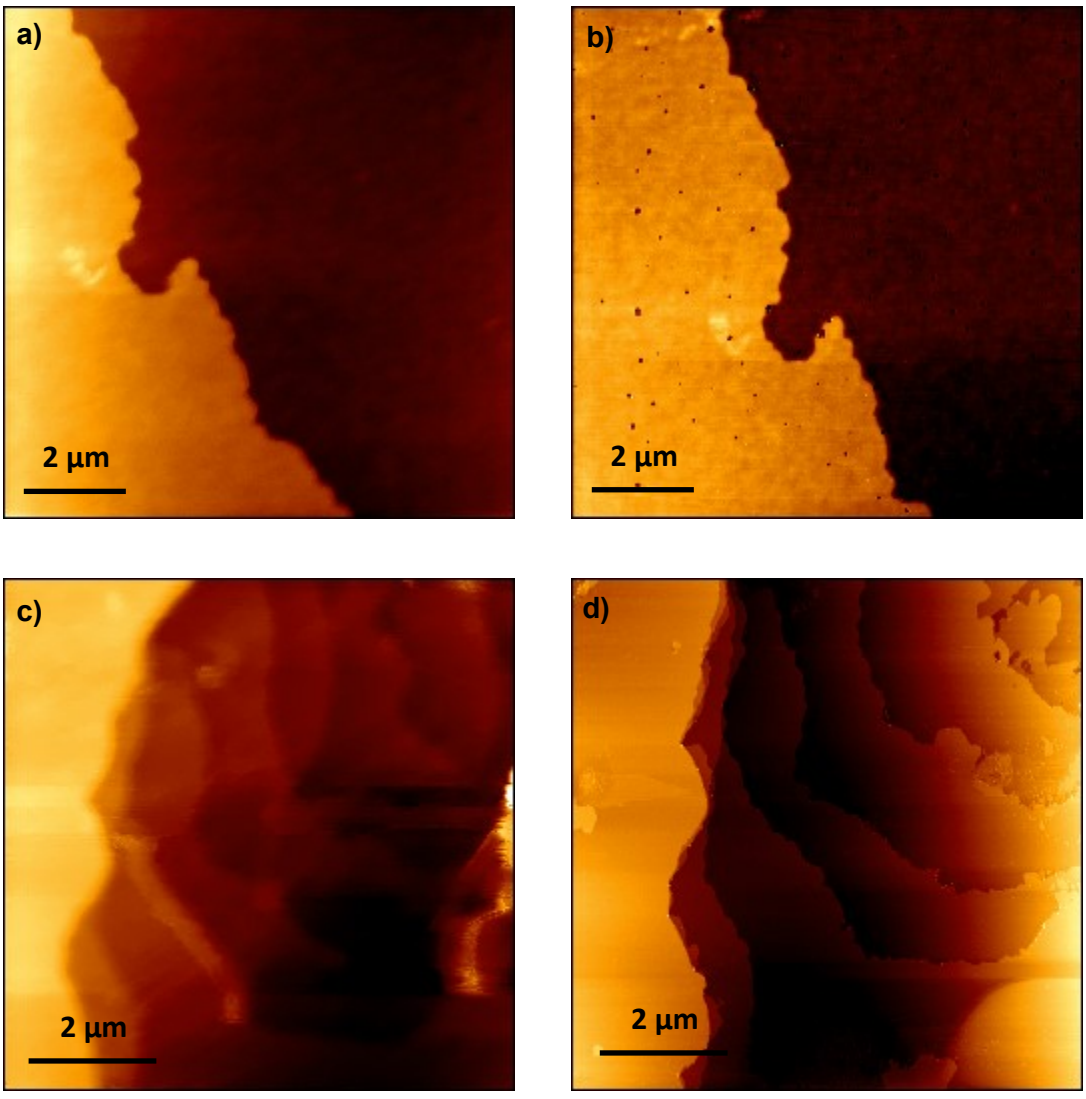

Figure S10. a) 10 x 10 µm² AFM micrographs of toluene-based liquid-liquid processed C8-BTBT-C8 thin films directly after deposition and b) after the aging process, c) 8 x 8 µm² AFM micrographs of heptane-based liquid-liquid processed C8-BTBT-C8 thin films directly after deposition and d) after the aging process.

S6 – NEXAFS fitting procedure and tilt angle derivation for fabricated thin films

S6-1 – General procedure

It is noted that extracted polar angles (α), tilt angles (β), and azimuthal angles (ϕ) refer to the rigid, conjugated BTBT core unit of the compound. The symmetrically attached alkyl chains are expected to be still flexible in the condensed phase. Experimental NEXAFS spectra were fitted using 13 Gaussian functions and 1 edge jump function (Fig. S11a). In case of azimuthal anisotropy (S6-3, S6-4), the considered early-π* intensities ($E_{Ph} \approx 285$ eV) are normalized to the largest overall intensity in any of the 3 spectra (Fig. 11b).

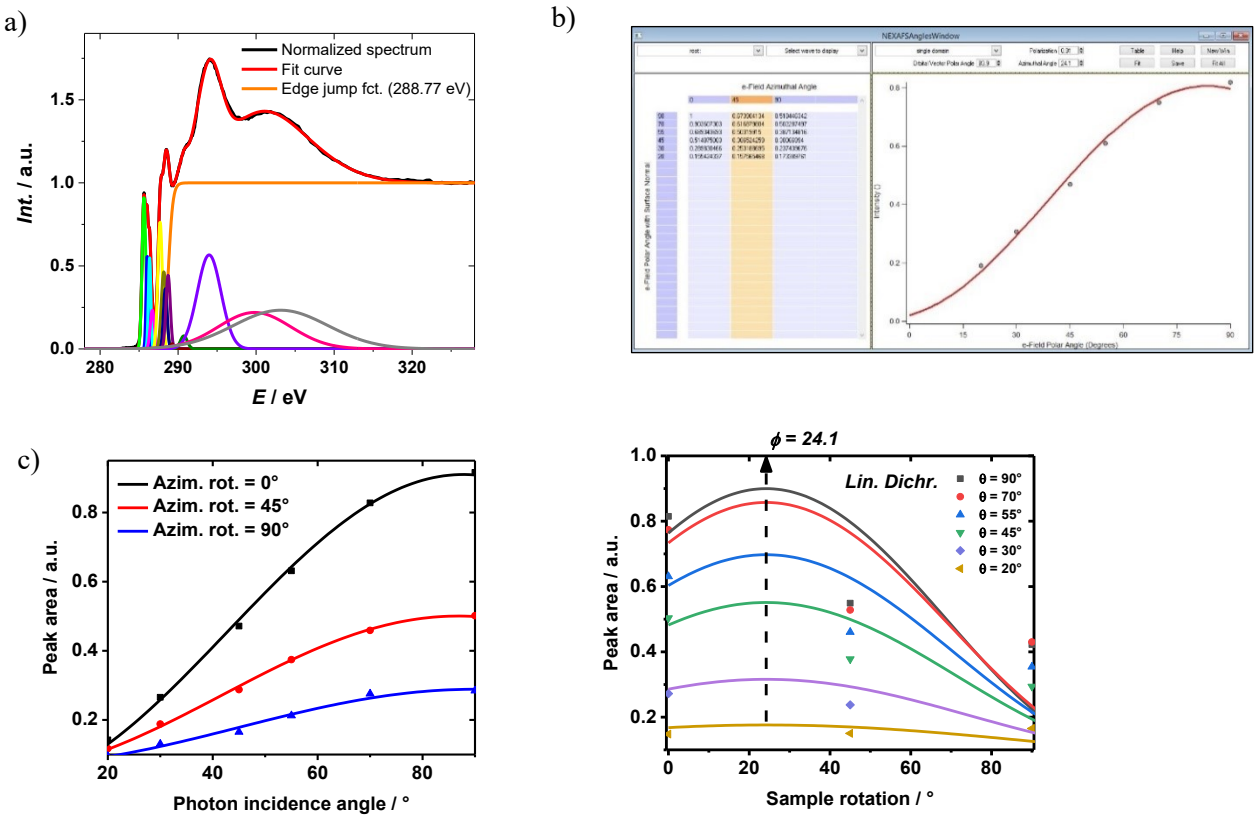

Figure S11. a) Representative angle dependent NEXAFS spectrum including fit function and sub-functions, b) exemplary screenshot of the applied fitting procedure, c) representation of the final fitting curves for a dataset containing 3 azimuthal (left) and 6 polar sample rotations (right).

S6-2 – Thermal evaporation

From STXM results (SI3-1), we expect no azimuthal dependency due to the presence of numerous azimuthally rotated domains merely excelling 10 µm within the probed film. Hence, only one (random) azimuthal angle was measured, and the polar and average tilt angle deduced.

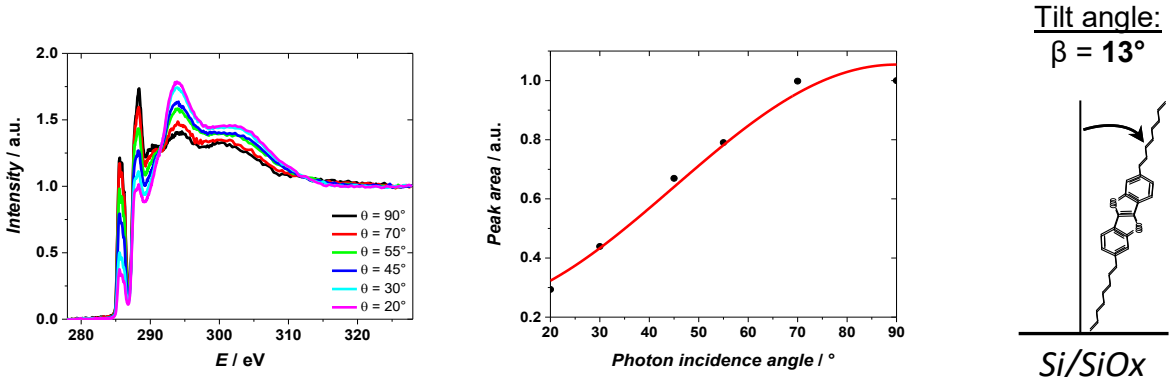

Figure S12. Full-range angle dependent NEXAFS spectrum (left), tilt angle derivation (middle) and averaged C8-BTBT-C8 orientation on the substrate surface for a thermally evaporated (d = 15 nm) thin film (right).

S6-3 – Dropcasting

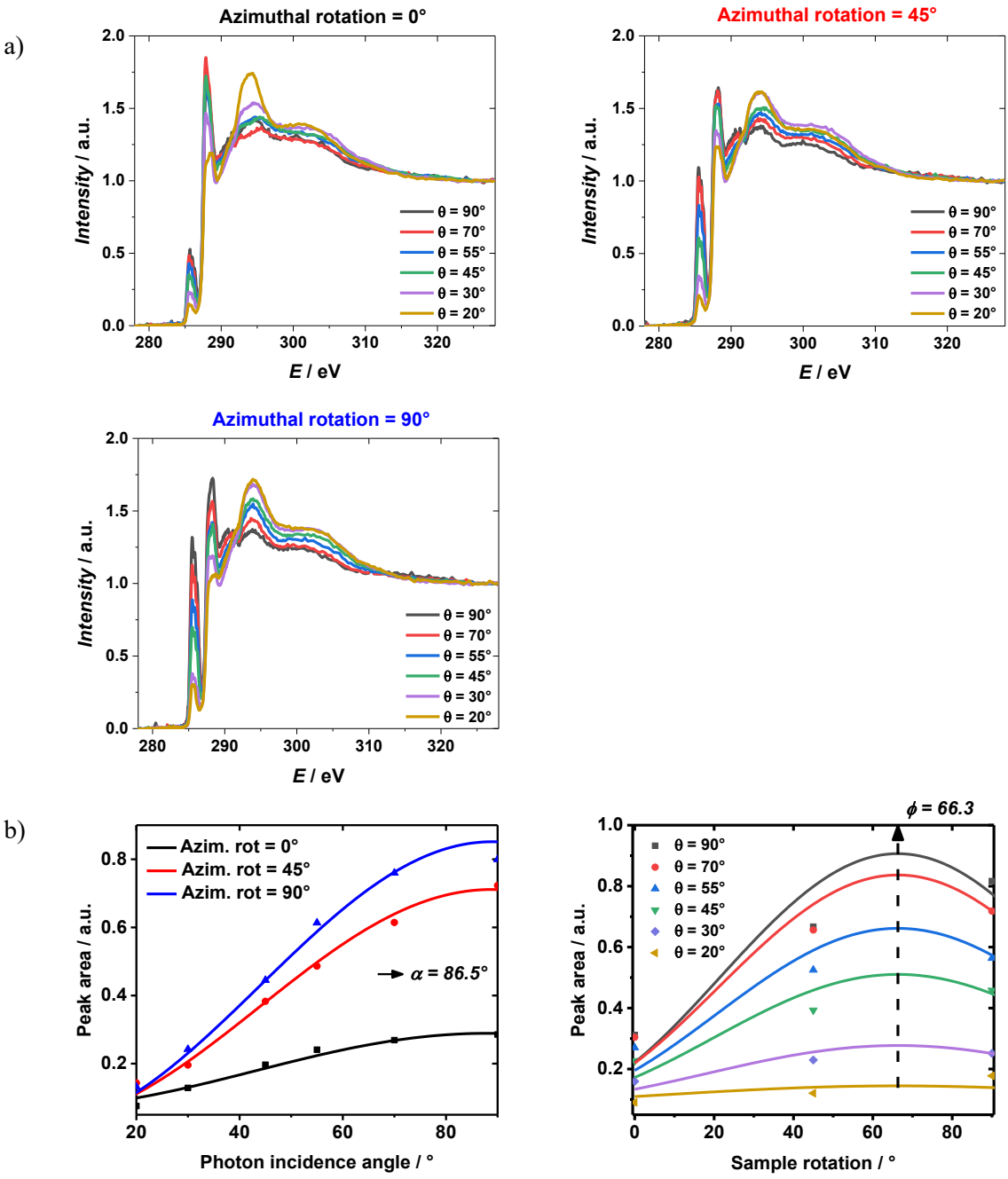

Figure S13. a) Full-range angle dependent NEXAFS spectra at various azimuthal rotations and b) representation of the final fitting curves for a dataset containing 3 azimuthal (left) and 6 polar sample rotations (right).

S6-4 – Liquid-liquid processing

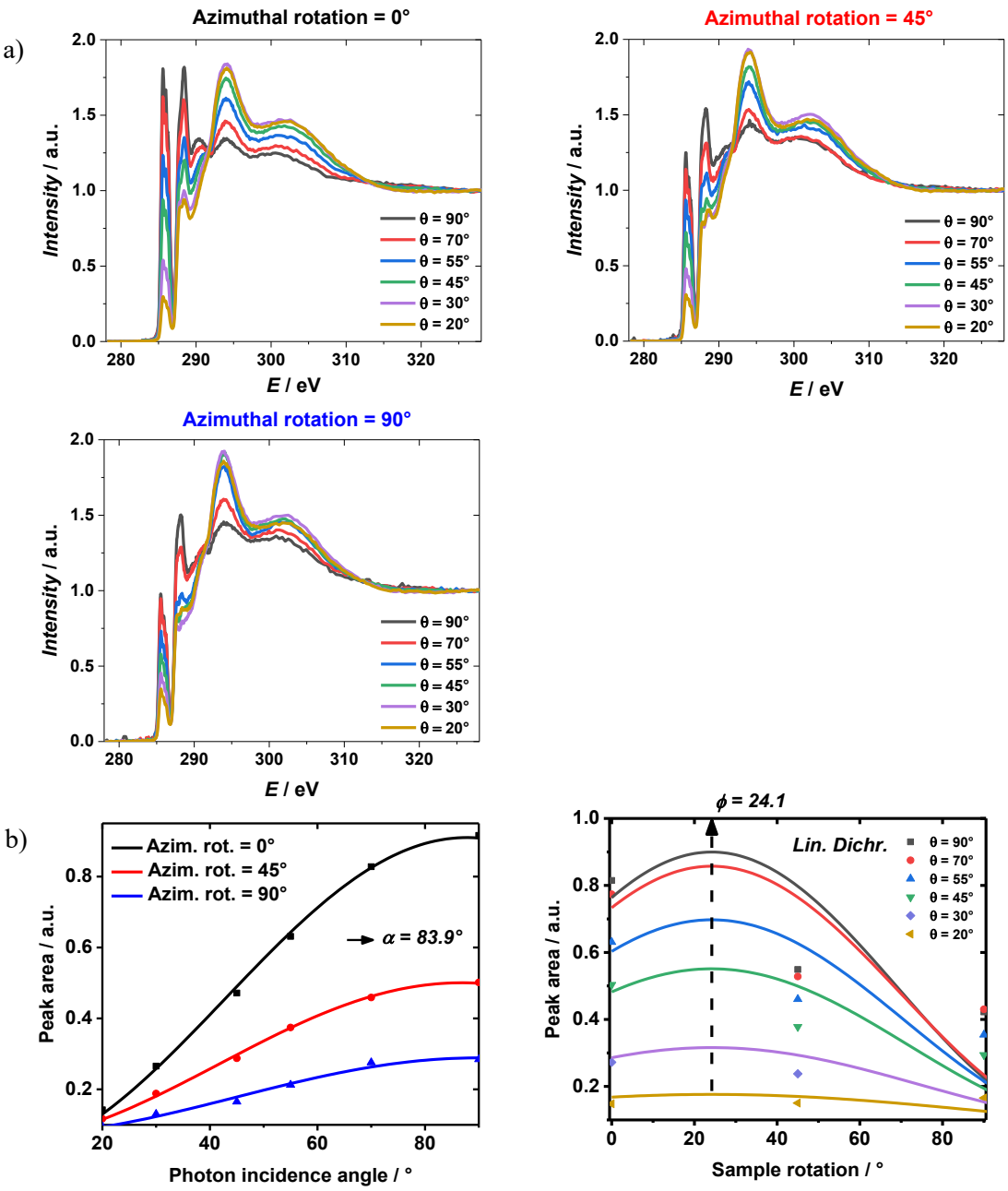

Figure S14. a) Full-range angle dependent NEXAFS spectra at various azimuthal rotations and b) representation of the final fitting curves for a dataset containing 3 azimuthal (left) and 6 polar sample rotations (right).